

Three-Dimensional Modeling and Simulation of Muscle Tissue Puncture Process

zongkai lv

Shandong University

qinghua song (✉ ssinghua@sdu.edu.cn)

Shandong Univeristy <https://orcid.org/0000-0002-9792-9988>

fan gao

Shandong University

zhanqiang liu

Shandong University

yi wan

Shandong University

yonghang jiang

University of Strathclyde

Original Article

Keywords: Puncture biopsy, Muscle soft tissue, 3D Puncture Simulation

Posted Date: May 20th, 2021

DOI: <https://doi.org/10.21203/rs.3.rs-532040/v1>

License:   This work is licensed under a Creative Commons Attribution 4.0 International License.

[Read Full License](#)

Version of Record: A version of this preprint was published at Chinese Journal of Mechanical Engineering on April 18th, 2022. See the published version at <https://doi.org/10.1186/s10033-022-00719-y>.

Title page

Three-dimensional Modeling and Simulation of Muscle Tissue Puncture Process

Zong-Kai Lv, born in 1998, is currently a master candidate at *Key Laboratory of High Efficiency and Clean Mechanical Manufacture (Ministry of Education), Shandong University, China*.

E-mail: lvzongkaisdu@163.com

Qing-Hua Song, born in 1982, is currently a professor at *Key Laboratory of High Efficiency and Clean Mechanical Manufacture (Ministry of Education), Shandong University, China*. He received his PhD degree on Mechanical Manufacturing and Automation in *Shandong University, China*, in 2009.

Tel: +86-531-88392539; E-mail: ssinghua@sdu.edu.cn

Fan Gao, born in 1996, is currently a master candidate at *Key Laboratory of High Efficiency and Clean Mechanical Manufacture (Ministry of Education), Shandong University, China*.

Zhan-Qiang Liu, born in 1969, is currently a professor at *Key Laboratory of High Efficiency and Clean Mechanical Manufacture (Ministry of Education), Shandong University, China*.

E-mail: melius@sdu.edu.cn

Yi Wan, born in 1977, is currently a professor at *Key Laboratory of High Efficiency and Clean Mechanical Manufacture (Ministry of Education), Shandong University, China*. He received his PhD degree from *Shandong University, China*, in 2006.

Yong-Hang Jiang, born in 1995, is currently a PhD candidate at *University of Strathclyde, England*.

Corresponding author: Qing-Hua Song E-mail: ssinghua@sdu.edu.cn

Three-dimensional Modeling and Simulation of Muscle Tissue Puncture Process

Received June xx, 201x; revised February xx, 201x; accepted March xx, 201x

© Chinese Mechanical Engineering Society and Springer-Verlag Berlin Heidelberg 2017

Abstract: Needle biopsy is an important part of modern clinical medicine. The puncture accuracy and sampling success rate of puncture surgery can be effectively improved through virtual surgery. Because fewer puncture existing three-dimensional(3D) model, it is impossible to guide the operation under complicated working conditions, which limits the development of virtual surgery. In this paper, 3D simulation of muscle tissue puncture process is studied. Firstly, the parameters of muscle tissue are measured. Considering the fitting accuracy and calculation speed, the M-R model is selected. Subsequently, an accurate 3D dynamic puncture model is established. The failure criterion is used to define the breaking characteristics of the muscle, and the bilinear cohesion model defines the breaking process. Experiments with different puncture speeds are carried out through the built in vitro puncture platform. The experimental results are compared with the simulation results. The accuracy of the model is verified by the high degree of agreement between the two curves. Finally, the model under different parameters is studied. Analyze the simulation results of different puncture depths and puncture speeds. The 3D puncture model can provide a more accurate model support for virtual surgery and help improve the success rate of puncture surgery.

Keywords: Puncture biopsy • Muscle soft tissue • 3D Puncture Simulation

✉ Qing-Hua Song
ssinghua@sdu.edu.cn

¹ Key Laboratory of High Efficiency and Clean Mechanical Manufacture, Ministry of Education, School of Mechanical Engineering, Shandong University, Jinan, P.R. China

² National Demonstration Center for Experimental Mechanical Engineering Education, Shandong University, Jinan, P.R. China

1 Introduction

Minimally invasive puncture is playing an increasingly important role in clinical treatment. Compared with traditional treatment, puncture biopsy has the advantages of less trauma and faster recovery [1-3]. Virtual surgery is the combination of simulation modeling and virtual reality surgery to realize the simulation of the surgical process. With the continuous development of modern medicine and computer technology, virtual surgery technology has been more and more applied to puncture technology. Virtual surgery is beneficial for surgeons to increase the experience of surgical operation, improve the success rate of surgery to a certain extent, also provide technical support for the training of interns. It is the most key link to establishing a precise surgery simulation model in virtual surgery. An accurate model can improve the accuracy of the contact deformation between the instrument and the organ during the operation, and adapt to the operating environment in a variety of circumstances, then improve the quality of surgery, reduce the biological soft tissue trauma and achieve accurate localization.

In recent years, many scholars have devoted themselves to the modeling and simulation of the puncture process, and adopted more complex models or finite element analysis to predict and improve the offset of the target in the puncture process [4-6]. The effect of the coating on the puncture process was investigated [7]. However, an accurate three-dimensional finite element model was not established to verify these results. Naohiko et al. [8] designed and developed an internal multi-axis control needle, which can perform knee surgery. Wang et al. [9] conducted a study on the cutting characteristics of the tangential surface of pig loin tissue, revealing the relationship between stress and pain perception. Jiang et al. [10] studied the changes of the needle during puncture and discussed the insertion mechanism under different puncture

parameters. Misra et al. [11] carried out puncture experiments using needles with different inclination angles. Abayazid et al. [12] and Roesthuis et al. [13] established respectively a kinematics model and a mechanical model of the flexible needle for the puncture process, and based on these two models, a real-time prediction of the puncture trajectory of the needle was made. Larger errors occur when the needle is bent to a greater extent. Dimaio et al. [14] used the finite element method to divide the structure of tissue units, and studied the influence of different puncture depths on tissue deformation through experiment and simulation respectively. However, Dimaio used a rigid needle in his study, which does not bend and deform during puncture, resulted in a major difference from a flexible needle. Gao et al. [15] proposed a needle-tissue coupling model based on the improved local constraint method, and studied the changes of forces and displacements of each node in the tissue. Datla et al. [16] established a prediction model of puncture needle body deflection based on the functional principle, and this model can accurately predict the deflection force and deflection displacement of the flexible needle with an inclined tip when puncture tissue. Oldfield et al. [17] used a three-dimensional finite element quasi-static simulation model for analysis, and found that compared with traditional linear needle entry, multi-body needle partial feed puncture method or reciprocating needle entry puncture method resulted in smaller displacement error of the target. Wang et al. [18] and Jiang et al. [19] studied the puncture force and target error, and established the mathematical and finite element model of the puncture process.

With the development of virtual surgery and the advances in modern medicine, performing sound pre-operative planning can reduce the risks and increase the success rate of a procedure. A 3D dynamic puncture model with a high degree of accuracy can provide more opportunities for trial and error for the surgeon, as well as more realistic practice for the trainee. Current research on 3D puncture models is sparse, and muscle tissue models are less accurate in terms of material parameters, making it difficult to guide surgery in complex working conditions.

A more accurate 3D puncture model is established in this paper. Analyze the mechanical properties of muscle tissue through tensile and compression tests. A more suitable constitutive model is selected by fitting. In the process of establishing the 3D model, the fracture criterion and the bilinear cohesion model are used. An in vitro puncture platform is set up to perform in vitro puncture experiments. The accuracy of the model is verified by the

comparison between experimental results and simulation results. Research on 3D models under different puncture speeds and puncture depths. Analyze the results and summarize the law of change. Get better puncture parameters.

2 Materials and methods

2.1 Analysis of mechanical properties of soft tissue

Currently, muscle soft tissue is generally considered to be hyperelastic material due to its high similarity to rubber-like materials. Compared with muscle tissue and rubber, they are both in a linear structure, and the fiber and macromolecule chains are similar to the curling stage, which can be like in Figure 1 C (a), without an external force acting. Under external tensile force, the fiber and macromolecule chains become in order and show straighten linear stage like C (b). Along with the strain increases, the stress of muscle tissue firstly shows the linear increase and then become nonlinear increase until the muscle tissue completely straightens as shown in A. The difference between muscle tissue and rubber is that in the next stage of tensile shown in C (c), the muscle fiber will stop deformation due to the protection of the myolemma. To protect muscle fiber, accompanied strain deformation the myolemma will prior to starting plastic change and fracture than the muscle fiber as the red connected tissue is shown in C (3). Thus, the stress-strain curve of muscle tissue shows a linear stage when rubber material still shows nonlinear and its slope of the curve continues to increase. This is the reason that when using hyperelastic constitutive model matching muscle tissue always results in a less precise stress-strain curve.

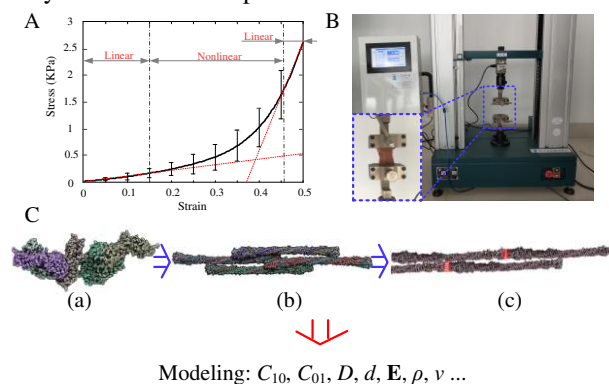


Figure 1 Stress-strain curve of tensile test

2.2 Muscle tissue modeling and tool modeling

Point at the above situation, a novel method for the constitutive model of muscle tissue is proposed by

dividing the stress-strain curve into three parts and respectively defining their mechanical characteristics. The assumption of three parts is according to the characteristic of the constitution of the muscle tissue and the characteristic of the stress-strain curve[20]. The first part of the curve is treated as hyperelastic material from the beginning of strain changing to the end of the nonlinear stage. The second part of the curve is regarded as plastic material due to the plastic deformation of the myolemma. The third part uses the fracture model to identify its mechanical characteristic.

The first part of the constitutive model of muscle tissue is a hyperelastic model. Most of the constitutive models of biological tissues are based on the continuum mechanics of isotropic and hyperelastic materials. That is, the strain energy density function depends on the strain invariants I_1 , I_2 , and J in the three right Cauchy-Green deformation tensors. If the elastomeric material is approximately incompressible, then I_3 is considered constant and equal to 1, which means that I_3 does not contribute to the strain energy. The most classical form of strain energy can be expressed as a polynomial made up of invariants.

$$W = W(\bar{I}_1, \bar{I}_2, J) = \sum_{i+j=N} C_{ij} (\bar{I}_1 - 3)^i (\bar{I}_2 - 3)^j + \sum_{i=1}^N \frac{1}{D_i} (J - 1)^{2i}, \quad (1)$$

where W is the strain energy function. I_1 , and I_2 are the first two right Cauchy-Green deformation tensors, respectively. J is the deformation gradient tensor. C_{ij} and D_i are the material constants.

Second Piola-Kirchhoff stress tensor \mathbf{S} can be derived by expressing the partial derivative of W concerning Cauchy-Green strain tensor \mathbf{E} or right Cauchy-Green tensor based on the chain rule,

$$\mathbf{S} = \frac{\partial W}{\partial \mathbf{E}} = \frac{\partial W}{\partial I_1} \frac{\partial I_1}{\partial \mathbf{E}} = 2 \frac{\partial W}{\partial I_1} \frac{\partial I_1}{\partial \mathbf{C}}, \quad (2)$$

$$= 2 \left[\frac{\partial W}{\partial I_1} I + (I_1 I - C) \frac{\partial W}{\partial I_2} + I_3 C^{-1} \frac{\partial W}{\partial I_3} \right]$$

The Cauchy stress tensor σ can be obtained by pushing forward \mathbf{S} ,

$$\sigma_h = \frac{1}{J} \mathbf{F} \cdot \mathbf{S} \cdot \mathbf{F}^T = \frac{2}{J} \left[\frac{\partial W}{\partial I_1} \mathbf{F} \cdot \mathbf{F}^T + (I_1 \mathbf{F} \cdot \mathbf{F}^T - \mathbf{F} \cdot \mathbf{F}^T \cdot \mathbf{F} \cdot \mathbf{F}^T) \frac{\partial W}{\partial I_2} + I_3 \frac{\partial W}{\partial I_3} I \right], \quad (3)$$

In the case of simple tests, such as uniaxial compression, biaxial compression and pure shear, the Cauchy stress tensor can be expressed by substituting deformation gradient $\mathbf{F} = \text{diag}(\lambda_1, \lambda_2, \lambda_3)$ and with simplification,

$$\sigma_h = \frac{2}{J} \left[\lambda_i^2 \frac{\partial W}{\partial I_1} + (I_1 \lambda_i^2 - \lambda_i^4) \frac{\partial W}{\partial I_2} + I_3 \frac{\partial W}{\partial I_3} \right] e_i \otimes e_i, \quad (4)$$

where the invariants are given by

$$\begin{aligned} I_1 &= \lambda_1^2 + \lambda_2^2 + \lambda_3^2 \\ I_2 &= \lambda_1^2 \lambda_2^2 + \lambda_2^2 \lambda_3^2 + \lambda_1^2 \lambda_3^2, \\ I_3 &= \lambda_1^2 \lambda_2^2 \lambda_3^2 \end{aligned} \quad (5)$$

Equation (2) can be written as the following direct stress components by Equation (3),

$$\begin{aligned} \sigma_{11} &= \frac{2}{J} \left[\lambda_1^2 \frac{\partial W}{\partial I_1} + (\lambda_2^2 \lambda_1^2 + \lambda_3^2 \lambda_1^2) \frac{\partial W}{\partial I_2} + I_3 \frac{\partial W}{\partial I_3} \right], \\ \sigma_{22} &= \frac{2}{J} \left[\lambda_2^2 \frac{\partial W}{\partial I_1} + (\lambda_1^2 \lambda_2^2 + \lambda_3^2 \lambda_2^2) \frac{\partial W}{\partial I_2} + I_3 \frac{\partial W}{\partial I_3} \right], \\ \sigma_{33} &= \frac{2}{J} \left[\lambda_3^2 \frac{\partial W}{\partial I_1} + (\lambda_1^2 \lambda_3^2 + \lambda_2^2 \lambda_3^2) \frac{\partial W}{\partial I_2} + I_3 \frac{\partial W}{\partial I_3} \right], \end{aligned} \quad (6)$$

where, λ_i is the principal stretch in the deformation phase and the soft tissue is assumed as isotropy during the deformation process, which means $I_3=1$.

Here, Mooney-Rivlin is chosen to regard as a hyperelastic constitutive model to describe the first part of deformation,

$$W = C_{10} (I_1 - 3) + C_{01} (I_2 - 3), \quad (7)$$

The M-R model retains two of the polynomials because the shear stress is proportional to the shear angle when the hyperelastic material is subjected to a simple shear load, which makes the model more accurate in tensile and shear experiments.

The second part of the constitutive model is the plastic model. The plastic stage refers to the deformation of the material under the action of an external force. When the applied external force disappears, the object cannot be restored to its original state. Due to the special characteristic of the hyperelastic material structure, the hyperelastic model does not include the plastic stage. This is because hyperelastic materials can maintain a large deformation state and it is difficult to determine the plastic stage, which means that it is difficult to guarantee the plastic stage. The last linear stage in A Fig.1 cannot be well fitted using the hyperelastic model, so this section is considered as the plastic stage. The plastic stage is linear and its formula is derived as follows.

As usual, the elastic-plastic model deformation can be divided into elastic deformation and plastic deformation.

The general form is as follows,

$$\mathbf{F} = \mathbf{F}^{el} \cdot \mathbf{F}^{pl}, \quad (8)$$

where \mathbf{F} is the total deformation gradient, \mathbf{F}^{el} is the total elastic gradient, \mathbf{F}^{pl} is the total plastic gradient. This formula can be rewritten when applied to hyperelasticity.

$$\mathbf{F} = \mathbf{F}^{hl} \cdot \mathbf{F}^{pl}, \quad (9)$$

where \mathbf{F}^{hl} is the total hyperelastic gradient. Decomposition of the deformation gradient in the above formula yields the decomposition rate in strain rate as follows,

$$\dot{\mathbf{E}} = \dot{\mathbf{E}}^{el} + \dot{\mathbf{E}}^{pl}, \quad (10)$$

where $\dot{\mathbf{E}}$ is the total strain rate, $\dot{\mathbf{E}}^{el}$ is the total superelastic strain rate, and $\dot{\mathbf{E}}^{pl}$ is the total plastic strain

rate. The hyperelastic strain rate can be solved by the strain energy density equation. In addition, in non-elastic flows, it is assumed that the yield limit is set to zero. In the non-elastic flow of material, the inelastic deformation part according to the definition of the flow rule can be expressed as follows,

$$d\varepsilon^{pl} = \sum_i d\lambda_i \frac{\partial g_i}{\partial \sigma}, \quad (11)$$

where, $g_i(\sigma, \theta, H_{i,a})$ is the potential energy, $d\lambda_i$ is the time change rate. According to the above method, the plastic stage stress and strain data are fitted to obtain the plastic stage model.

The third part of the constitutive model is the fracture model. After the plastic stage, muscle tissue begins to break. Due to the muscle tissue exhibiting overall shear damage while breaking, so shear failure is selected in the form of fracture damage. The stress-strain relationship in the fracture model is as follows,

$$\sigma = (1-d)D_0^{hl} : (\varepsilon - \varepsilon^{pl}) = D^{hl} : (\varepsilon - \varepsilon^{pl}), \quad (12)$$

where, D_0^{hl} indicates the hyperelastic stiffness at the beginning. D^{hl} is the hyperelastic degenerate stiffness, d is the stiffness degradation variable, which ranges in size from 0 (undamaged material) to 1 (completely destroyed material). Failure modes combined with failure criteria lead to a sharp decrease in the elastic stiffness, and the stiffness degradation is isomorphic and determined only by a single degenerate variable d . The available stress from continuous fracture mechanics is as follows,

$$\bar{\sigma} = D_0^{hl} : (\varepsilon - \varepsilon^{pl}), \quad (13)$$

Finally, Cauchy stress and finite stress are available through a degenerative relationship,

$$\sigma = (1-d)\bar{\sigma}, \quad (14)$$

2.3 Analysis of mechanical properties of soft tissue

2.3.1 Uniaxial tensile test

The universal testing machine is used to respectively carry out uniaxial tensile tests on the fibrous and vertical fibrous muscle tissue samples to obtain the stress-strain relationship in the process of deformation. To avoid the great difference between the normal deformation and the excessive stretching speed, a stretching speed of 5mm/min is adopted, which also ensures that the internal connective tissue does not break down rapidly due to rapid tension during the experiment. Tensile tests are carried out on the experimental tissue, and 8 groups of experiments are carried out along the fiber direction and the vertical fiber direction respectively. Standard deviation analysis and average ultimate strength stress calculation are carried out on the experimental data results. The solution of the

stress-strain relationship can be expressed by the following formula,

$$\sigma = \frac{F}{A}, \quad \varepsilon = \frac{L-L_0}{L_0} \quad (15)$$

where, σ is nominal stress. F is tensile force. A is the cross-sectional area of the sample. ε is nominal strain. L is the length after deformation. L_0 is the initial length of the sample.

The average stress-strain curve obtained after processing the experimental data from multiple experiments is shown in Figure 2. Figure 3 shows the muscle tissue tensile states along with the fiber direction and the vertical fiber direction at stress maximum respectively.

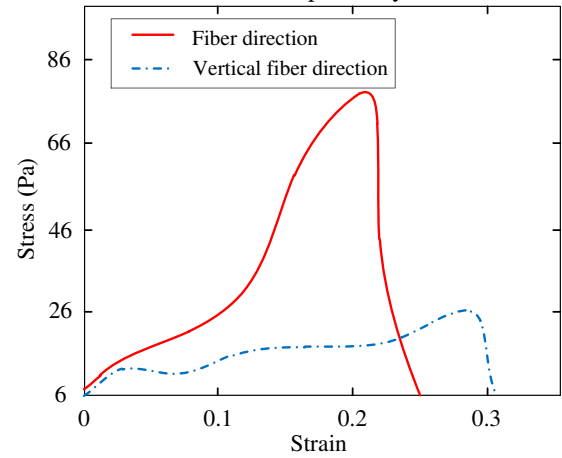


Figure 2 Stress-strain curve in different tensile directions

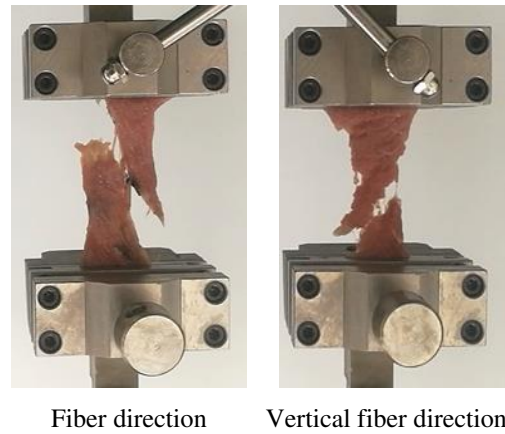


Figure 3 Fracture state in different tensile directions

It can be seen from Figure 2 that the maximum stress of muscle tissue stretching along the fiber direction is much greater than that of muscle tissue stretching along the vertical fiber direction. The strain at fracture is slightly larger in the vertical fiber direction than in the fiber direction. Taking the average value of the ultimate stress measured from the 8 groups of experiments, it can be

obtained that the average value of the ultimate stress is 0.085MPa along the fiber direction, and 0.026MPa along the vertical fiber direction. The ultimate stress along the fiber direction is larger than that along the vertical fiber direction, which is about 3.2 times of it.

2.3.2 Uniaxial compression test

The universal testing machine is used to carry out the compression test, and the test samples similar to the tensile test are taken, except the compression fixture is replaced, and 6 groups of the same compression tests are carried out. The force and displacement data obtained from the experiments are processed by Equation (15), and the stress-strain curve as shown in the figure is obtained.

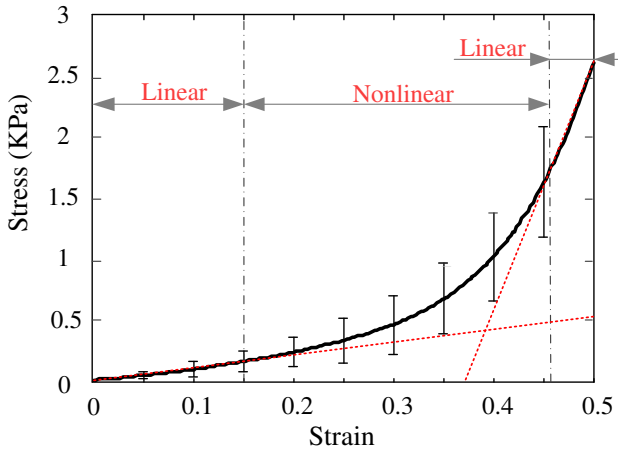


Figure 4 Stress - strain curve in compression experiment

As shown in Figure 4, due to the individual differences of samples during the experiment, the results of the 6 groups of experiments are averaged and the error line is made by means of mean \pm variance for the stress at the same strain.

According to the stress-strain curve, the compression process can be divided into three stages. The first stage is the stage of small deformation, in which the stress-strain curve is linear and the stress increases slowly with the increase of strain. The stress-strain curves of the second stage show the nonlinear law. In the third stage, the stress-strain curve shows linear rule again, and the stress increases rapidly with the increase of strain.

2.3.3 Parameter fitting in the hyperelastic stage

In the finite element analysis of biological soft combinations, they are generally regarded as hyperelastic bodies. In order to better select suitable superelastic constitutive equations, different superelastic constitutive equations are used to fit the stress-strain curves in Figure 4. The fitting results of different hyperelastic constitutive

equations are shown in Figure 5.

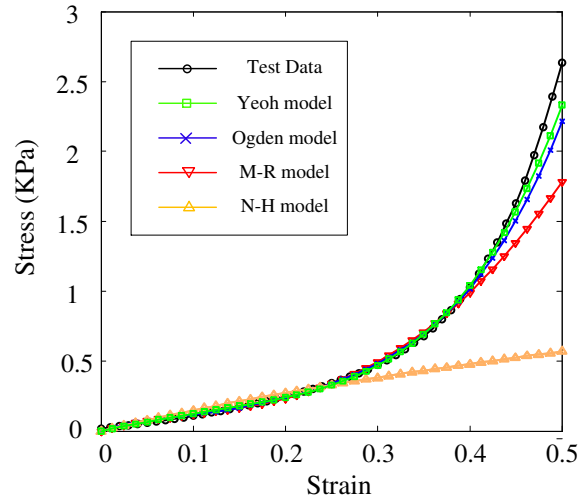


Figure 5 Fit results of different hyperelastic models to experimental data

It can be seen from Figure 5 that the linearly, non-linearly and linear stress-strain curves obtained by experiments are greatly different from those obtained by fitting. It can be seen that in the nonlinear stage, due to the characteristics of the single material constant, some experimental data of the N-H model deviated. M-R model also has the problem of insufficient accuracy in the nonlinear stage.

Due to the small strains in soft tissues, the third linear stage is generally not reached. In order to construct an accurate deformation model for soft tissues and to simplify the number of calculations, the third linear stage is discarded. The superelastic model of linear - nonlinear phase is fitted here. The composition of the two-order material constants of the M-R model makes it perform well in the small deformation of hyperelastic materials. Under the condition of ensuring the accuracy of the first two stages, the M-R model is selected for curve fitting.

In the simulation of muscle tissue puncture, the stiffness degradation variable is set as 0.95 and the failure displacement is set as 4×10^{-006} . The displacement criterion is used when setting fault evolution. For the softening model, the linear softening is used and maximum recession is set for recession mode. The initial linear slope is 1140, and the final linear slope is 20000.

Table 1 Material Constants

C_{10}	C_{01}	D	d	$E(\text{MPa})$	$\rho (\text{g}/\text{mm}^3)$	ν
4.75	-4.91	4×10^{-6}	0.95	640000	1.48×10^{-8}	0.22

In this work, the material constants are matched by the above method, and the final result can be shown in Table.1. The last three parameters are the material constants of the

scalpel.

3 Finite element model

3.1 Geometric models and material properties

The performance of tissues is complex and diverse, and there are many changes in muscle tissues during the puncture process. The complex changes are one of the important factors affecting the simulation accuracy, which also leads to the difficulty in establishing a high-quality model. The 3D simulation model of the needle biopsy process is established in ABAQUS by using the display solver. This model can save computation time and reduce computation amount. When setting the material attribute parameters, the values obtained from the previous experimental data are used to ensure accuracy to a certain extent.

For muscle tissue, M-R hyperelastic model is selected to better describe the deformation behavior. For some of its material property parameters, the equivalent Young's modulus is set as 20GPa and the Poisson's ratio is set as 0.495. The needle is placed above the model of muscle tissue. The puncture needle is given a speed of 2 mm/s to penetrate the muscle tissue model vertically at a constant speed.

3.2 Contact and boundary conditions

In the definition of the contact algorithm, the whole set is to allow the objects to contact each other. For some key areas of contact, surface contact is used to define more accurately. The muscle tissue model is set as fixed coupling to avoid the influence of muscle tissue movement in the direction of the puncture needle tube on the puncture process. To avoid excessive component deformation, the friction coefficient between the needle and the muscle tissue is defined as 0.3, and the friction at the tip of the needle is set as no friction. The mesh division of the organization model is arranged to ensure the accuracy and efficiency of operation. As shown in Figure 6, in the area where the muscle tissue is in contact with the puncture needle, the approximate global size of the mesh in this area is set to 0.8. From this area to the edge, the mesh size gradually increases. The approximate global size of the puncture needle model is set as 1. The unit types of the model are all C3D48. To simulate the contact fracture between the tissue and the puncture needle more accurately, a bilinear cohesion model is also introduced.

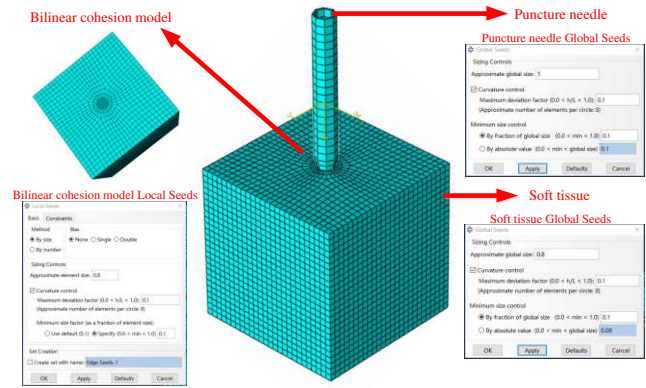


Figure 6 3D simulation model

4 Results analysis and discussion

4.1 Analysis of 3D simulation results

The puncturing process of three-dimensional puncture simulation is shown in Figure 7. As can be seen from Figure 7, the stress change of puncture needle and tissue is relatively insignificant. The stress variation area is mainly in the contact area between the puncture needle and the tissue, and the stress variation is in a circular distribution. Stress concentration occurred in the contact between tissue and puncture needle, and the stress in tissue is greater than that in tissue edge due to the extrusion of deformation. According to the stress scale, the change of stress is smaller beyond the tissue edge, which is consistent with the actual situation of puncture surgery.

To verify the accuracy of the 3D model, in vitro puncture experiments are required to compare with the simulation. As soft tissues are susceptible to force degeneration and are not easily fixed, a specific in vitro puncture test platform is built to ensure that the puncture tests are carried out smoothly. As shown in Figure 8, the puncture motion platform consists of a precision motion platform and a fixed base. A 6-axis mechanics sensor is mounted in the center of the fixed base and a puncture needle base connects the puncture needle to the six-axis mechanic's sensor. This allows the movement of the sliding table to be controlled by the controller, which drives the needle to perform the puncture. The soft tissue fixation box holds the soft tissue in place and prevents the soft tissue from moving during the puncture process. Due to the small force on the puncture needle, a signal amplifier is required to amplify the signal from the sensor.

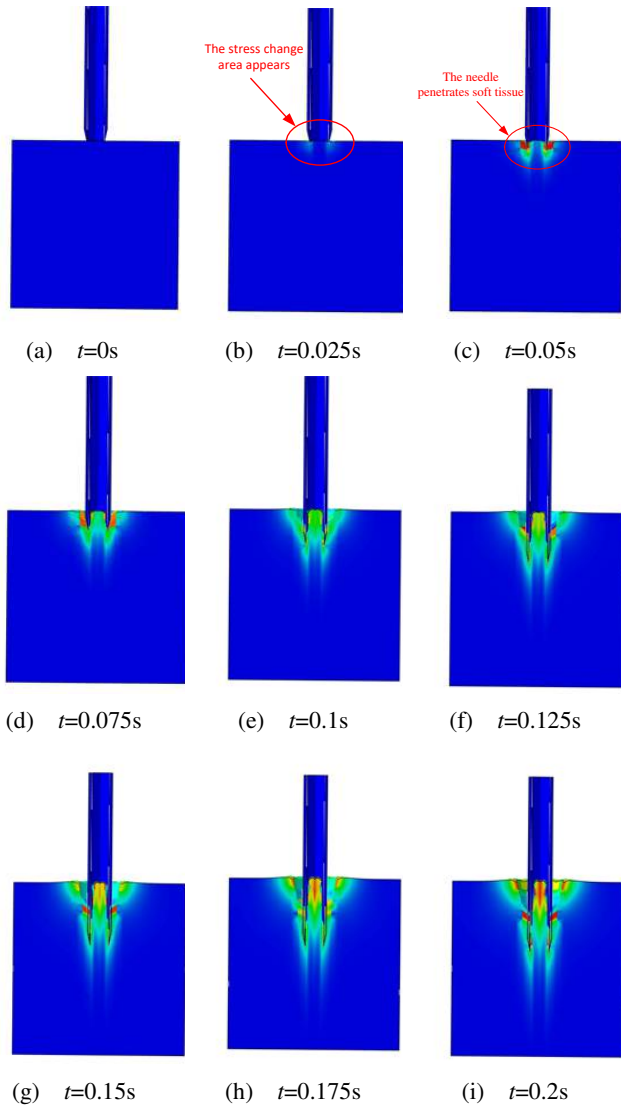


Figure 7 Stress changes during puncture

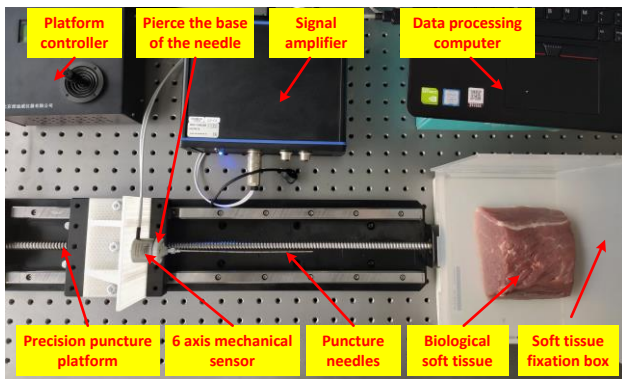


Figure 8 Top view of the extracorporeal puncture experimental platform

4.2 3D simulation results of different puncture depths

To analyze the stress of different puncture depths and

puncture needles, three stages in the process of complete puncture simulation are intercepted. The three stages are the first contact between the puncture needle and soft tissue, the tip of the needle entering the tissue, and the puncture needle penetrates the soft tissue 5mm. As shown in Figure 9, the mechanical properties of soft tissue hyperelasticity make the puncture needle protrude both externally and internally. The small space inside the needle leads to the extrusion pressure from the inner wall of the needle to the center of the needle in the process of puncture. The deformation of soft tissue inside the needle is more severe than that outside the needle. When the puncture reaches a certain depth, there is enough friction between the inner wall of the needle and the internal tissue. When the puncture needle exits the tissue, it takes the internal tissue to separate from the original whole, to achieve the purpose of puncture biopsy.

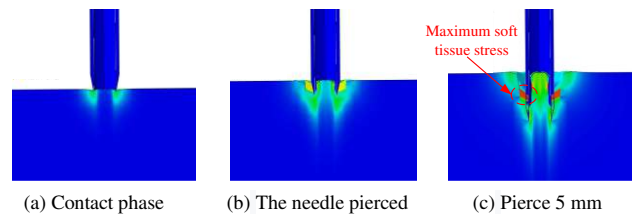


Figure 9 Stress changes at different puncture depths

Because the force on the muscle tissue is difficult to measure, the reaction force of the puncture needle is the same as the force on the muscle tissue. When we analyze the force on the muscle tissue, we analyze the reaction force of the puncture needle. Figure 10 shows the reaction force of the puncture needle during puncture. The tip of the needle touching the outer membrane of the soft tissue is counted as the starting point of the puncture process. Before point X, the needle tip has not been able to penetrate the soft tissue due to the rigidity of the biological valve. The puncture needle increases as the puncture depth increases, until it punctures the biological valve. After point X, the puncture needle pierces the outer membrane of the soft tissue, and the reaction force drops suddenly. At this time, the needle tip will damage the soft tissues, making the needle tip more stressful. The part behind the needle tip rubs against the soft tissue, making the stress of this part smaller than the needle tip. The reaction force is regarded as the combined force of the cutting force of the needle tip on the soft tissue and the friction force received by the outer wall of the needle. As the puncture depth increases, the frictional force increases, and the reaction force also increases.

The stress curve in Figure 10 is not smooth. As the puncture depth increases, multiple sudden drops appear on

the stress curve. The ideal curve should be a linear curve. It is preliminarily speculated that the reason for this phenomenon is due to the unevenness of the muscle and soft tissue. If a uniform tissue prosthesis is punctured, there are only two sudden drops of force, one at the moment of piercing the soft tissue and the other at the moment of piercing the tissue. In the following discussion of different puncture speeds, it will be further analyzed through experiments.

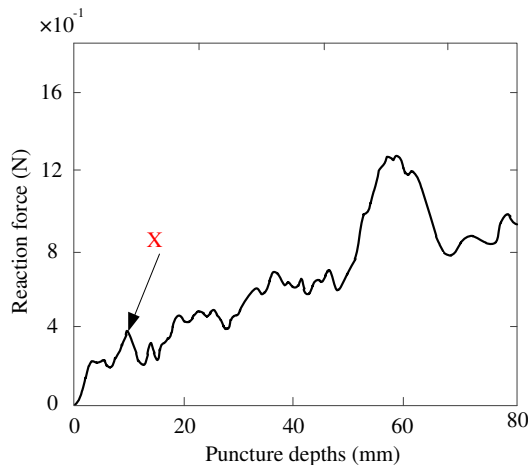


Figure 10 Reaction force of puncture needle at different puncture depths

4.3 3D simulation results of different puncture speeds

To analyze the stress changes at different puncture speeds, 4 groups of simulations with puncture depths of 3mm, 6mm, 9mm and 12mm are designed in Figure 11. The puncture depth of each group is the same, and the puncture velocities from left to right are 2mm/s, 5mm/s and 10mm/s, respectively. As can be seen from Figure 11, with the increase of puncture speed, the fitting degree between the outer wall tissue and the puncture needle gradually decreases, and the stress change increases. The fitting degree of the internal tissue of the puncture needle and the puncture needle decreases and the strain increases. The higher the fit of the puncture needle to the tissue, the greater the puncture resistance and the more likely it is that tissue adhesions will occur, which can cause secondary wound injury. Therefore, maintaining a high puncture speed within a certain range during puncture is beneficial in reducing tissue damage and increasing the rate of wound healing.

As shown in Figure 12, Figures A, B and C show the experimental and simulation controls for puncture velocities of 2mm/s, 5mm/s and 10mm/s respectively. The

maximum values of the simulated reaction forces in Figures A, B and C are 1.28N, 1.21N and 1.36N respectively. The maximum values of the experimental reaction forces are 1.35N, 1.33N and 1.36N respectively.

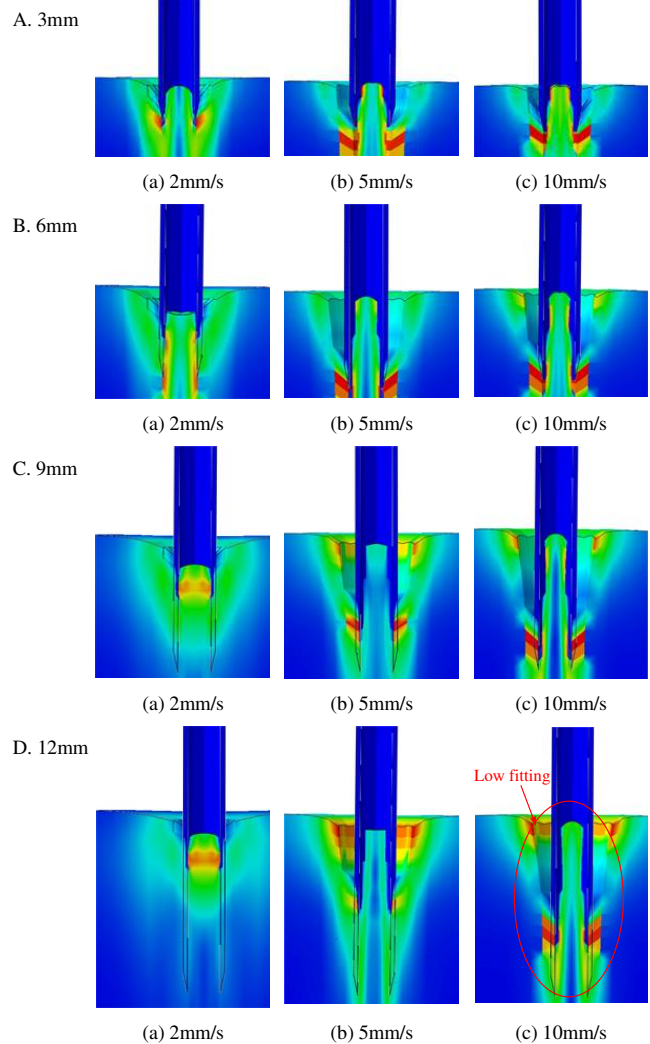


Figure 11 Stress changes at different puncture speeds at 3mm, 6mm, 9mm, 12mm

It can be seen from Figure 12 that during the puncture process, the stress curve has multiple sudden drops. Through experimental analysis, the reasons for this phenomenon can be divided into two types. One is the vibration of the puncture needle during the puncture process, and the other is caused by the interaction between the tissue and the puncture needle. The degree of sudden drop caused by the interaction between the tissue and the puncture needle is greater than the degree of sudden drop caused by needle vibration. When analyzing the interaction between the tissue and the puncture needle, it is analogous to the process of cutting the workpiece with the tool. During the cutting process of the tool, some

high-temperature chips will form a built-up edge on the tool edge. During the puncture process, due to the stickiness of the soft tissue, part of the soft tissue adheres to the needle tip, forming a soft tissue "built-up edge".

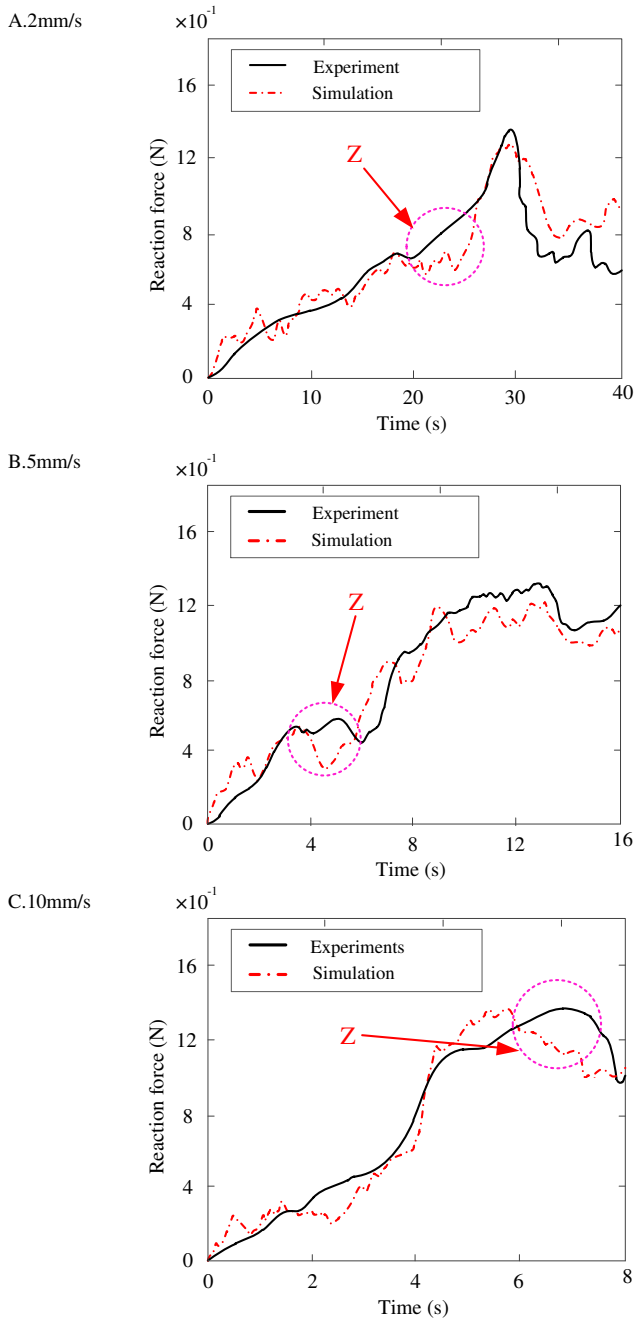


Figure 12 Reaction force of puncture needle at different puncture speeds

Due to the existence of "built-up edge" in soft tissues, the reaction force curve shows a non-linear growth. When the "built-up edge" disappears, there will be a sudden drop point. During the puncture process, the phenomenon

of "built-up edge" also continuously produced, disappeared and reproduced. The frequency of occurrence determines the number of sudden drop points during the puncture process. With the increase of the puncture speed, the frequency of the occurrence and disappearance of "built-up edge" also increased, so that the sudden drop points also increased, and the puncture stability of the needle decreased.

As shown in area Z in Figure 12, there is a certain deviation between the experimental data and the simulation results. During the experiment, the puncture needle can be seen as a cantilever structure fixed at one end, which is affected by its own gravity. The puncture platform inevitably produces small amplitude vibration during the puncture process. Due to the influence of equipment limitations and experimental environmental factors, certain errors appear between simulation and experimental data. It can be seen from Figure 12 that the experiment and simulation curves have a high degree of coincidence, and the above-mentioned error influence is small and can be ignored.

5 Conclusions

This paper studies finite element simulation of the interaction between flexible puncture needle and muscle tissue and establishes a high-precision 3D dynamic puncture model for characteristics of muscle tissue. The main contributions of this study are listed as follows:

- (1) An efficient method of modelling muscle tissue composition is proposed for the properties of muscle tissue. The stretching, compression and stress relaxation experiments of muscle tissue are carried out and the complex mechanical properties of muscle tissue are analyzed. By fitting multiple constitutive models, the M-R model is adopted to simulate and determine the characteristic parameters of each stage of muscle tissue. The results show that M-R model takes into account both fitting accuracy and calculation speed.
- (2) An accurate 3D dynamic puncture model is established. In the process of building 3D model, experimental data is are used to set soft tissue parameters. Bilinear cohesive force model is used to define the fracture during puncture contact. This can improve the calculation speed of the model on the premise of ensuring the accuracy. The failure criterion is adopted for the fracture characteristics of muscle tissue materials. The accuracy of the model is verified by comparing the results of in vitro puncture experiment with the simulation results. The accuracy and practical

application value of the 3D model is much higher than that of the 2D model

- (3) The puncture model under different parameters is studied. Larger puncture speed and smaller puncture depth can reduce wound damage. Puncture force increases with puncture depth. The greater the puncture speed, the more stress change points, and the stability of puncture will also decrease. The analysis of the 3D model has a positive effect on surgical design, surgical simulation, muscle tissue additive manufacturing, and bionic tissue design.

6 Declaration

Acknowledgements

Not applicable.

Funding

Supported by Natural Science Foundation of Shandong Province (Grant No. ZR2019JQ19) and the interdisciplinary research project of Shandong University (Grant No. 2017JC027)

Availability of data and materials

The datasets supporting the conclusions of this article are included within the article.

Authors' contributions

The author' contributions are as follows: Q H Song, Z Q Liu was in charge of the whole trial; Z K Lv, Q H Song, Y Wan wrote the manuscript; Z K Lv did the experimental verification; F Gao, Y H Jiang assisted with sampling and laboratory analyses.

Competing interests

The authors declare no competing financial interests.

Consent for publication

Not applicable

Ethics approval and consent to participate

Not applicable

References

- [1] G Gandaglia, K R Ghani, A Sood, et al. Effect of minimally invasive surgery on the risk for surgical site infections: results from the National Surgical Quality Improvement Program (NSQIP) Database. *Jama Surgery*, 2016, 149(10): 1039.
- [2] N Hansen-Algenstaedt, M K Kwan, P Algenstaedt, et al. Comparison between minimally invasive surgery and conventional open surgery for patients with spinal metastasis: A prospective propensity score-matched study. *Spine*, 2017, 42(10): 789-797.
- [3] G Dieberg, N A Smart, N King. Minimally invasive cardiac surgery: A systematic review and meta-analysis. *International Journal of Cardiology*, 2016, 223:554-560.
- [4] H Ramezanzpour, H Yousefi, M Rezaei, et al. Effects of rotational motion in robotic needle insertion. *Journal of Biomedical Physics & Engineering*, 2015, 5(4): 207-216..
- [5] T W Yang, H Yin, X G Zhao, et al. Interaction modeling and simulation of a flexible needle insertion into soft tissues. *Proceedings of the 45th International Symposium on Robotics*, Munich, Germany, June 3-6, 2014: 611-616.
- [6] Z Q Cheng, M Chauhan, B L Davies, et al. Modelling needle forces during insertion into soft tissue. *Conf Proc IEEE Eng Med Biol Soc*, 2015, 37(11):4840-4844.
- [7] F Gao, Q H Song, Y H Jiang, et al. Influence of a biocompatible hydrophilic needle surface coating on a puncture biopsy process for biomedical applications. *Coatings*, 2020, 10(2): 178.
- [8] N Sugita, Y Nakajima, M Mitsuishi, et al. Cutting tool system to minimize soft tissue damage for robot-assisted minimally invasive orthopedic surgery. *Proceedings of the international conference on medical image computing & computer-assisted intervention*, Springer-Verlag, 2007: 994-1001.
- [9] D Q Wang, Q H Song, Z Q Liu, et al. Cutting characteristics of porcine tenderloin tissue along tangential direction of surface. *International Journal of Advanced Manufacturing Technology*, 2017, 98(5): 1-11.
- [10] Y H Jiang, Q H Song, F Gao, et al. Needle deformation in the process of puncture surgery: experiment and simulation. *Proceedings of the 4th CIRP Conference on BioManufacturing 2019*, Guangdong, China, December 12-15, 2020, 270-276.
- [11] S Misra, K B Reed, B W Schafer, et al. Mechanics of flexible needles robotically steered through soft tissue. *International Journal of Robotics Research*, 2010, 29(13): 1640-1660.
- [12] M Abayazid, R J Roesthuis, R Reilink, et al. Integrating deflection models and image feedback for real-time flexible needle steering. *IEEE Transactions on Robotics*, 2013, 29(2): 542-553.
- [13] R J Roesthuis, M Abayazid, S Misra. Mechanics-based model for predicting in-plane needle deflection with multiple bends. *Proceedings of the 4th International Conference of the IEEE RAS/EMBS*, Roma, Italy, June 24-27, 2012: 69-74.
- [14] S P Dimaio, S E Salcudean. Needle insertion modeling and simulation. *IEEE Transactions on Robotics and Automation*, 2003, 19(5): 864-875.
- [15] D D Gao, Y Lei, B Yao. Dynamic soft tissue deformation estimation based on energy analysis. *Chinese Journal of Mechanical Engineering* (2016).
- [16] DATLA N V, KONH B, HONARVAR M, et al. A model to predict deflection of bevel-tipped active needle advancing in soft tissue[J]. *Med Eng Phys*, 2014, 36(3): 285-293.
- [17] N V Datla, B Konh, M Honarvar, et al. A model to predict deflection of bevel-tipped active needle advancing in soft tissue. *Medical Engineering & Physics*, 2014, 36(3):285-293.
- [18] M J Oldfield, A Leibinger, T E T Seah, et al. Method to reduce target motion through needle-tissue interactions. *Annals of Biomedical Engineering: The Journal of the Biomedical Engineering Society*, 2015.
- [19] X J Wang, J Shan. Study of the targeting error for percutaneous needle insertion into soft phantom material. *Journal of Mechanics in Medicine & Biology*, 2016, 16(02): 413-431.

- [20] G Chagnon, M Rebouah, D Favier. Hyperelastic energy densities for soft biological tissues: A review. *Journal of Elasticity*, 2015, 120(2): 129-160.

Biographical notes

Zong-Kai Lv, born in 1998, is currently a master candidate at *Key Laboratory of High Efficiency and Clean Mechanical Manufacture (Ministry of Education), Shandong University, China*.

E-mail: lvzongkaisdu@163.com

Qing-Hua Song, born in 1982, is currently a professor at *Key Laboratory of High Efficiency and Clean Mechanical Manufacture (Ministry of Education), Shandong University, China*. He received his PhD degree on Mechanical Manufacturing and Automation in *Shandong University, China*, in 2009.

Tel: +86-531-88392539; E-mail: ssinghua@sdu.edu.cn

Fan Gao, born in 1996, is currently a master candidate at *Key Laboratory of High Efficiency and Clean Mechanical Manufacture (Ministry of Education), Shandong University, China*.

Zhan-Qiang Liu, born in 1969, is currently a professor at *Key Laboratory of High Efficiency and Clean Mechanical Manufacture (Ministry of Education), Shandong University, China*.

E-mail: melius@sdu.edu.cn

Yi Wan, born in 1977, is currently a professor at *Key Laboratory of High Efficiency and Clean Mechanical Manufacture (Ministry of Education), Shandong University, China*. He received his PhD degree from *Shandong University, China*, in 2006.

Yong-Hang Jiang, born in 1995, is currently a PhD candidate at *University of Strathclyde, England*.

Appendix

Appendix and supplement both mean material added at the end of a book. An appendix gives useful additional information, but even without it the rest of the book is complete: In the appendix are forty detailed charts. A supplement, bound in the book or published separately, is given for comparison, as an enhancement, to provide corrections, to present later information, and the like: A yearly supplement is issue

Figures

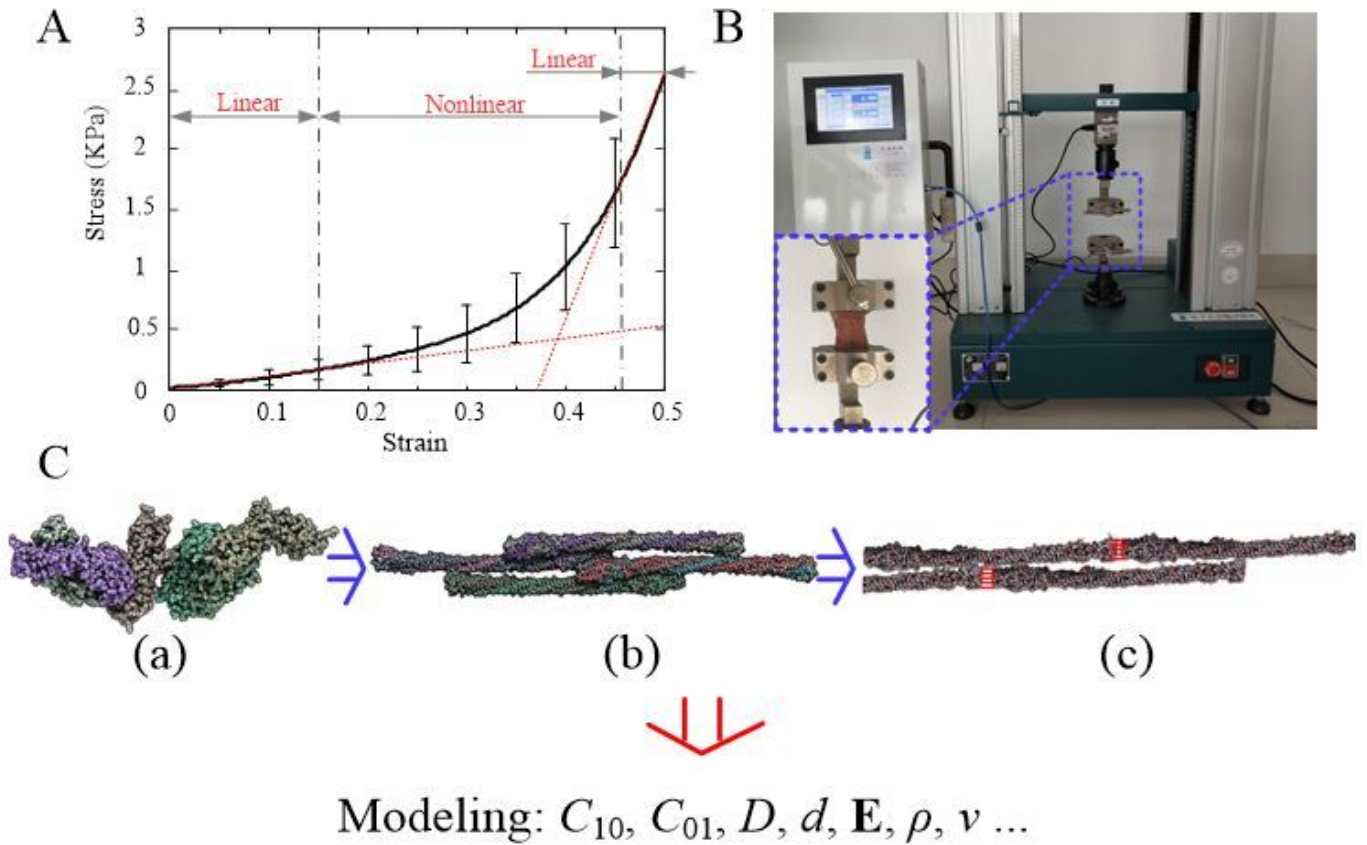


Figure 1

Stress-strain curve of tensile test

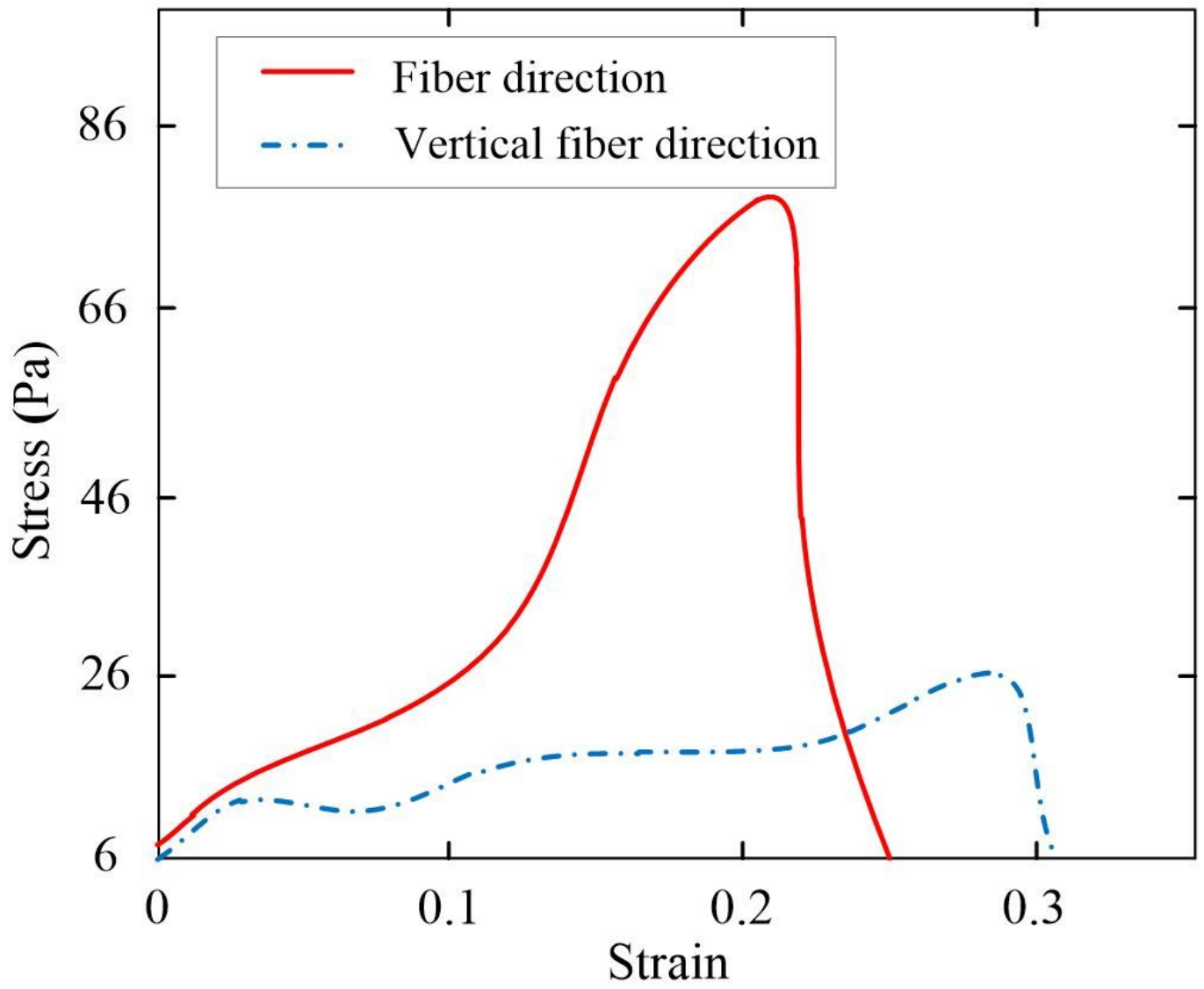


Figure 2

Stress-strain curve in different tensile directions



Fiber direction



Vertical fiber direction

Figure 3

Fracture state in different tensile directions

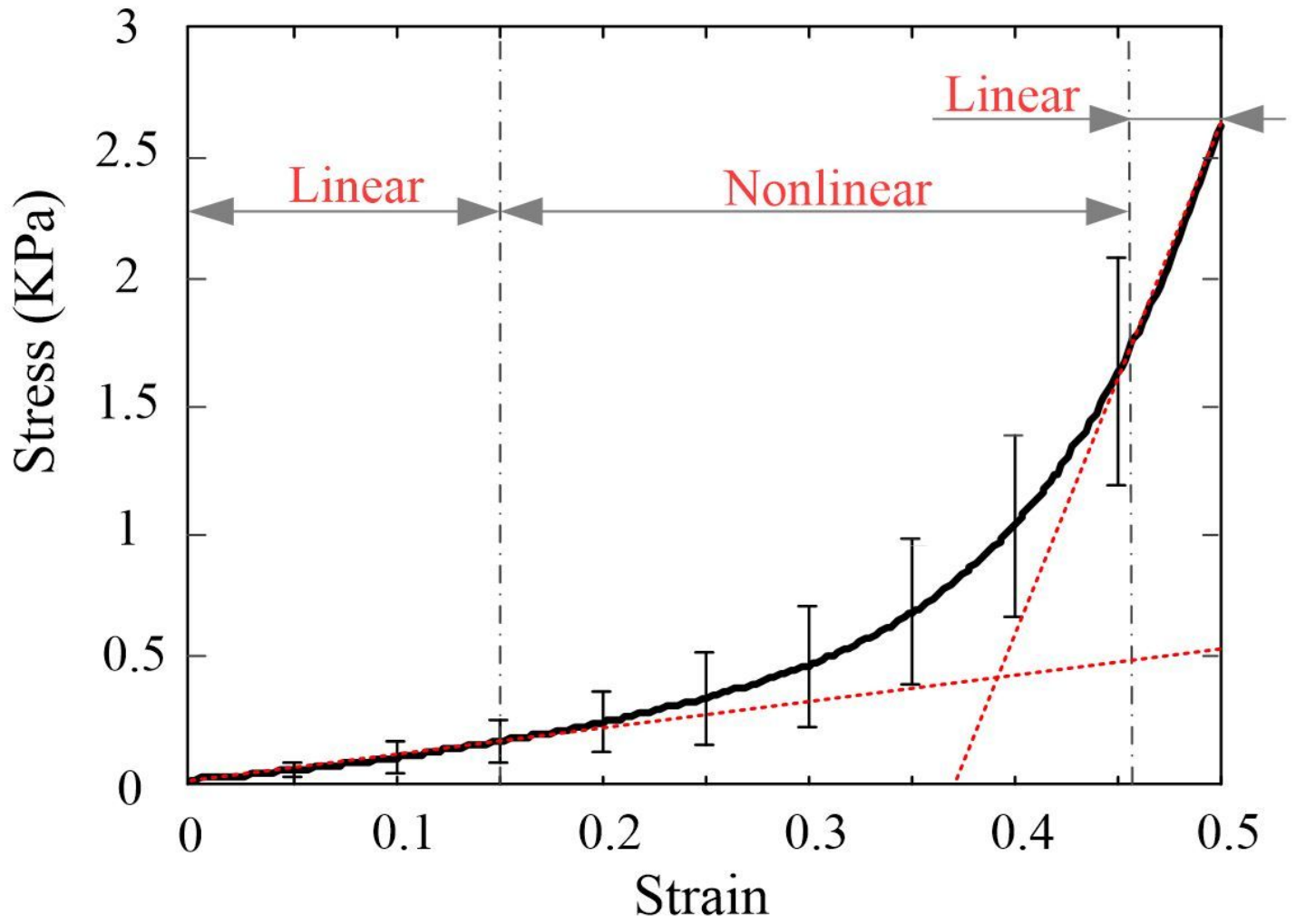


Figure 4

Stress - strain curve in compression experiment

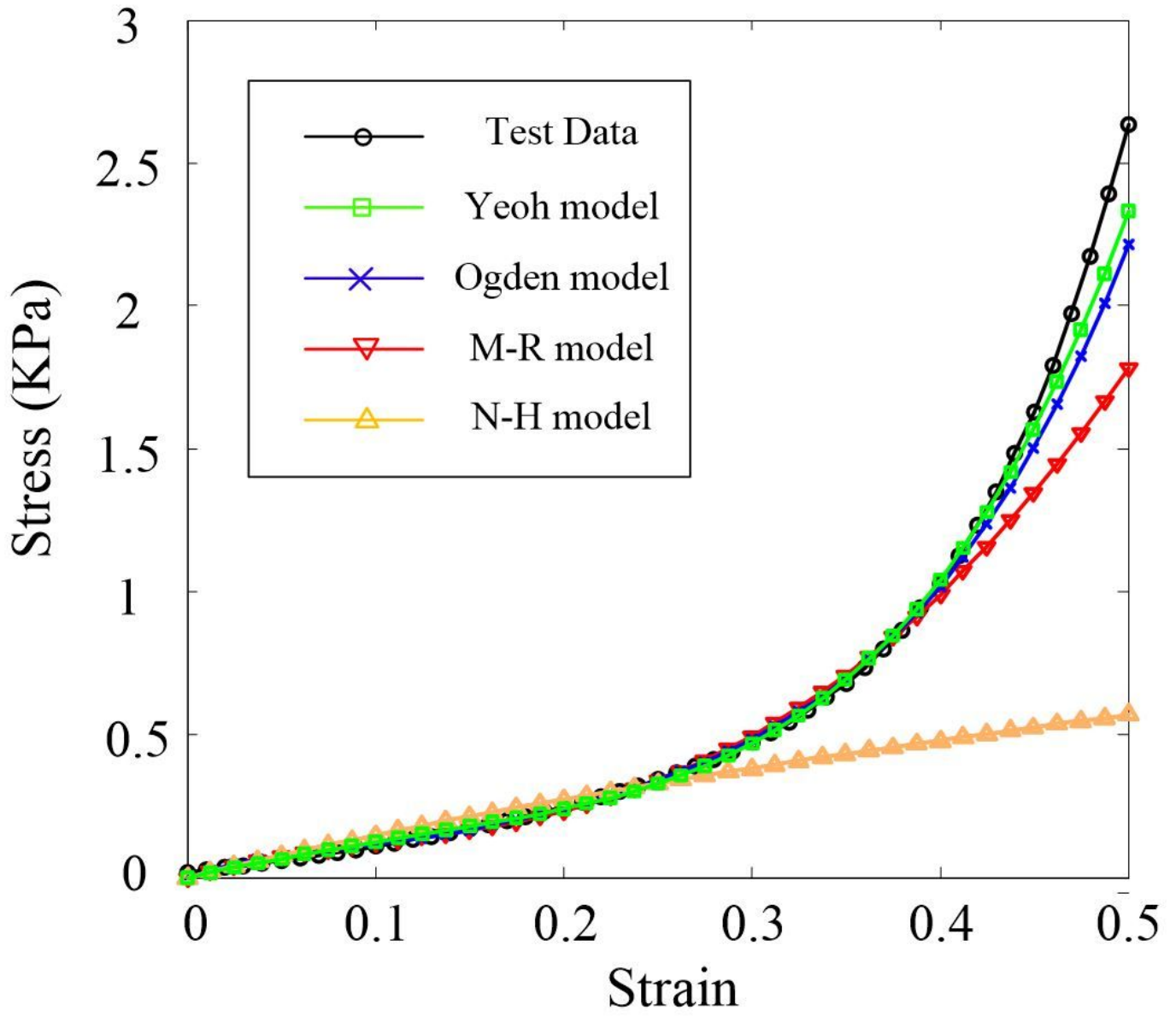


Figure 5

Fit results of different hyperelastic models to experimental data

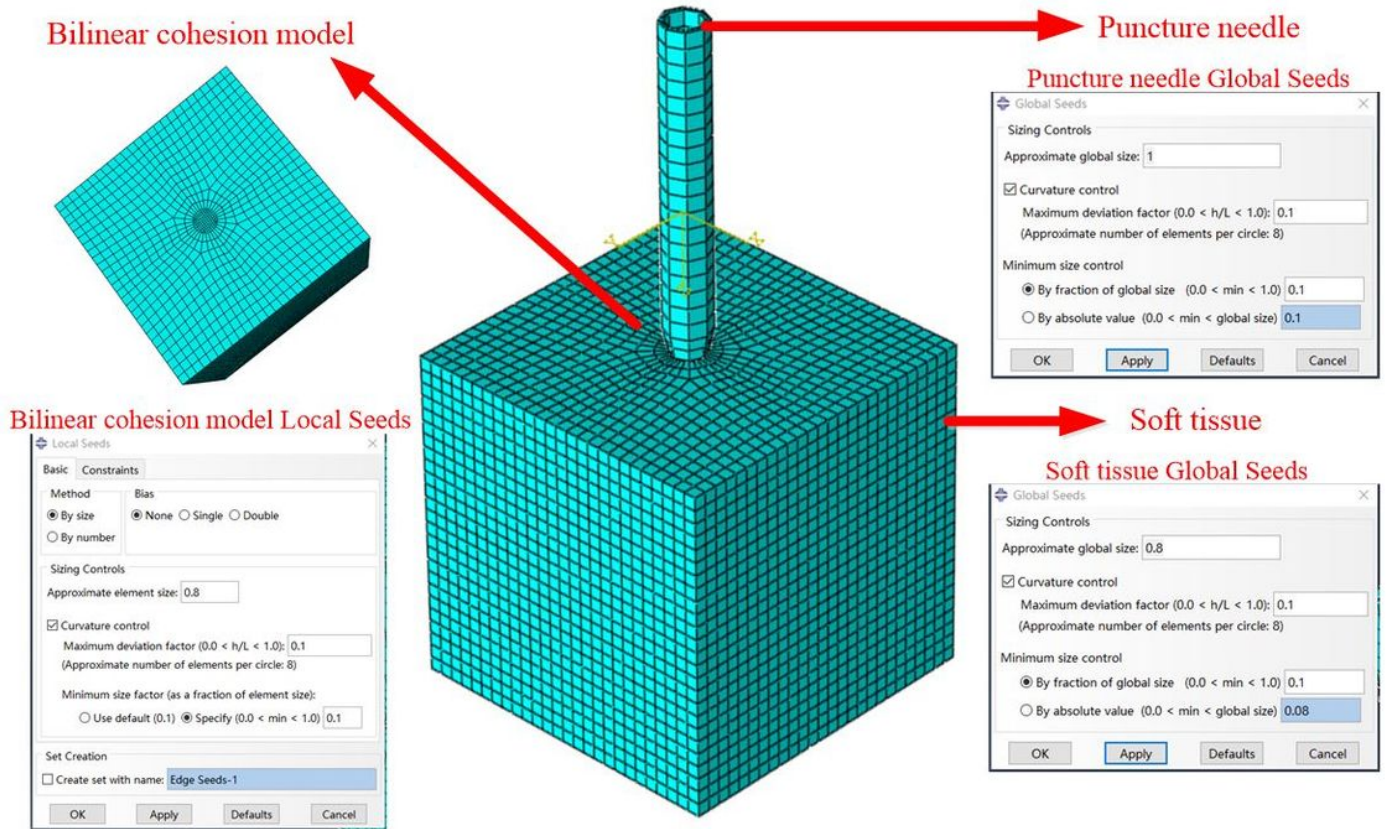


Figure 6

3D simulation model

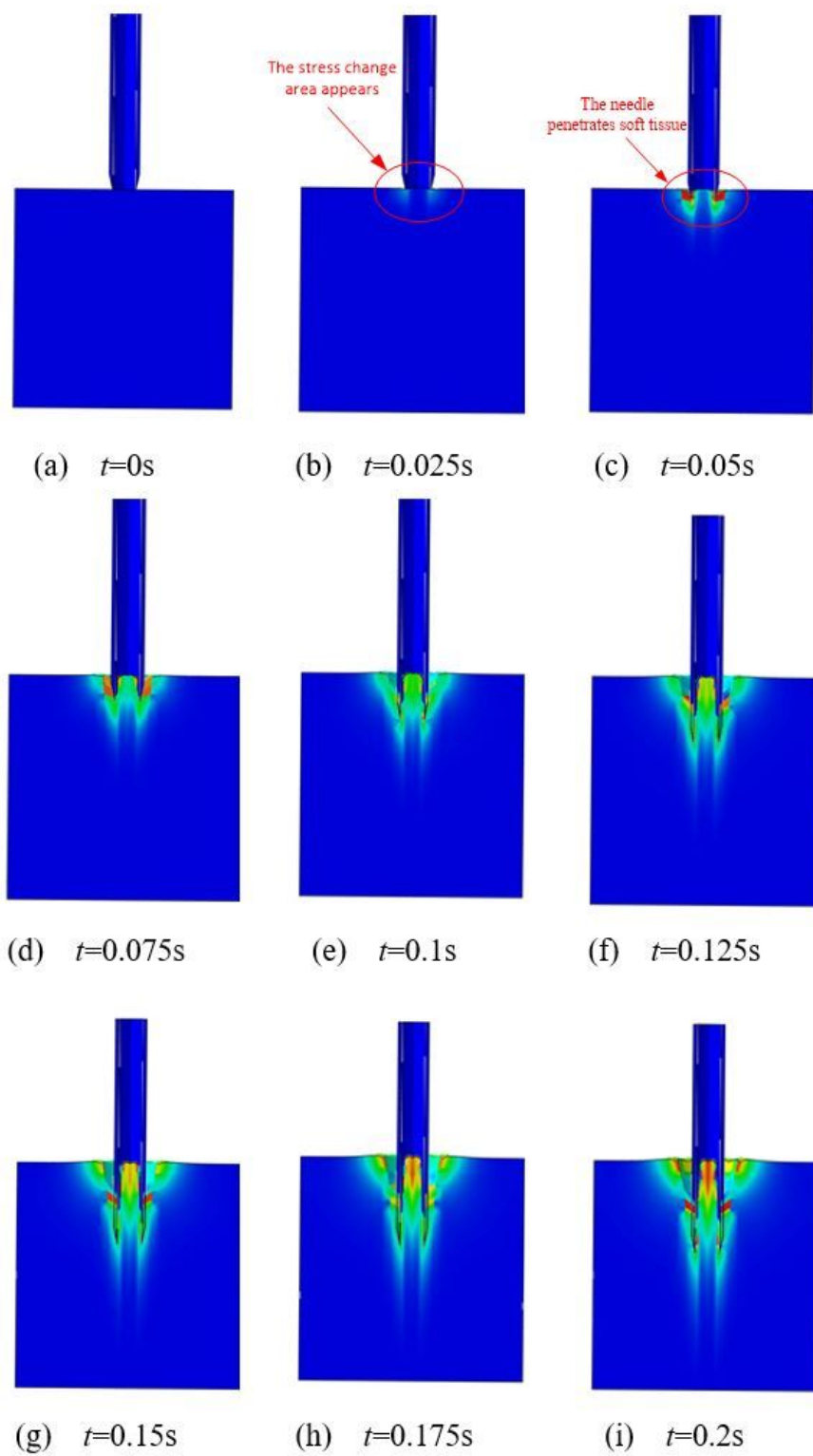


Figure 7

Stress changes during puncture

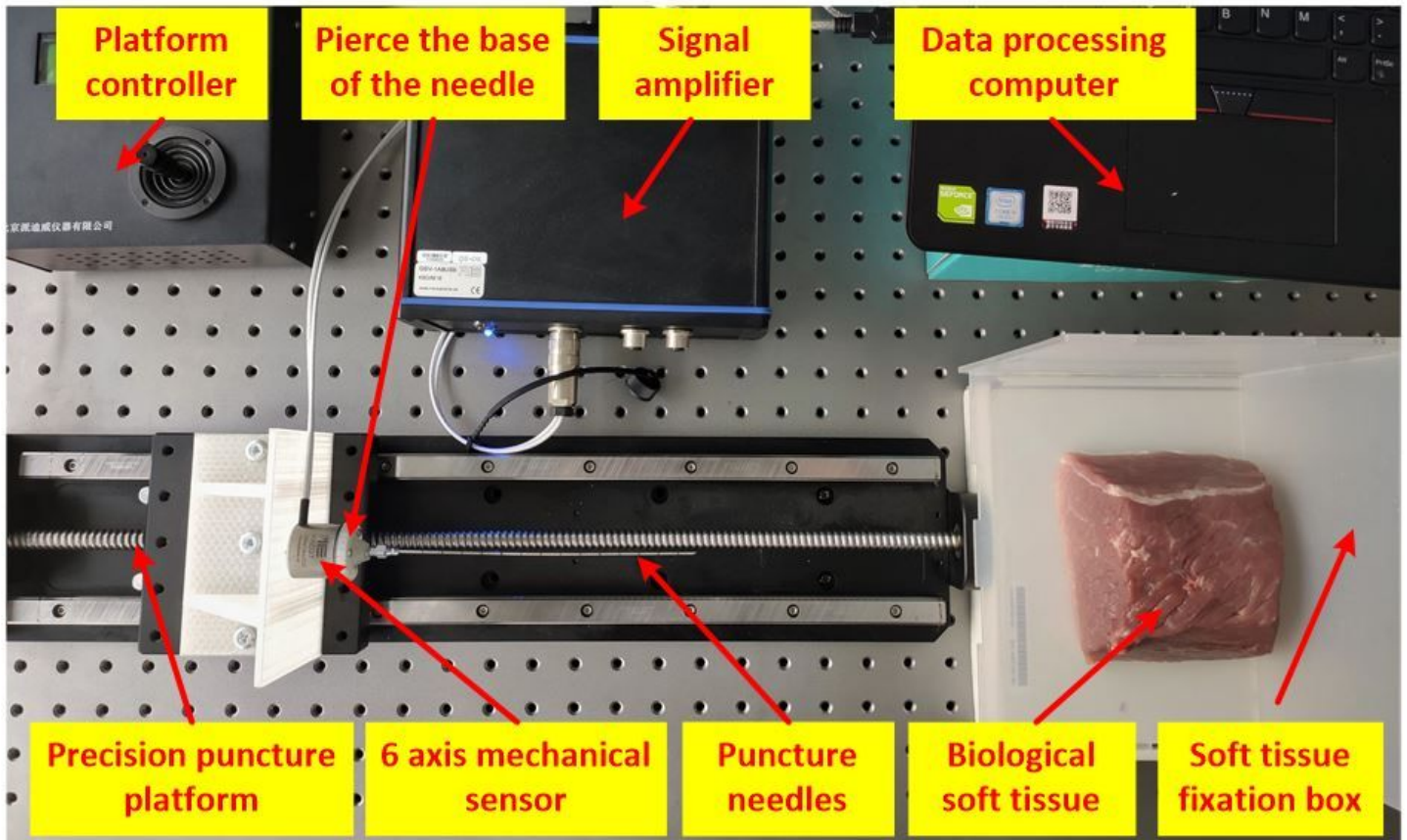


Figure 8

Top view of the extracorporeal puncture experimental platform

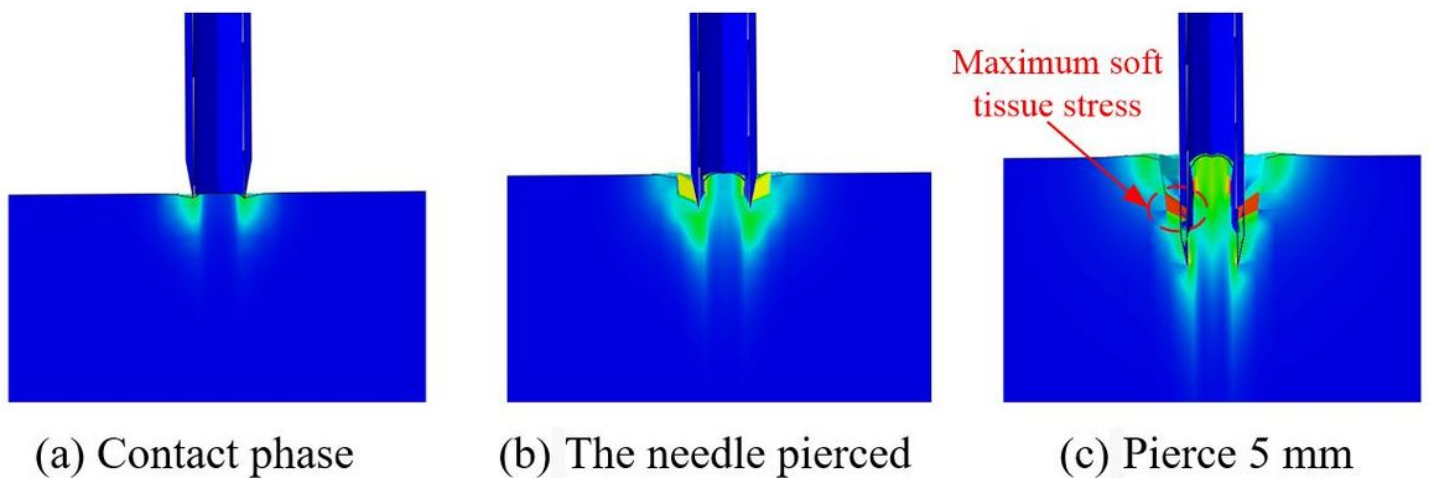


Figure 9

Stress changes at different puncture depths

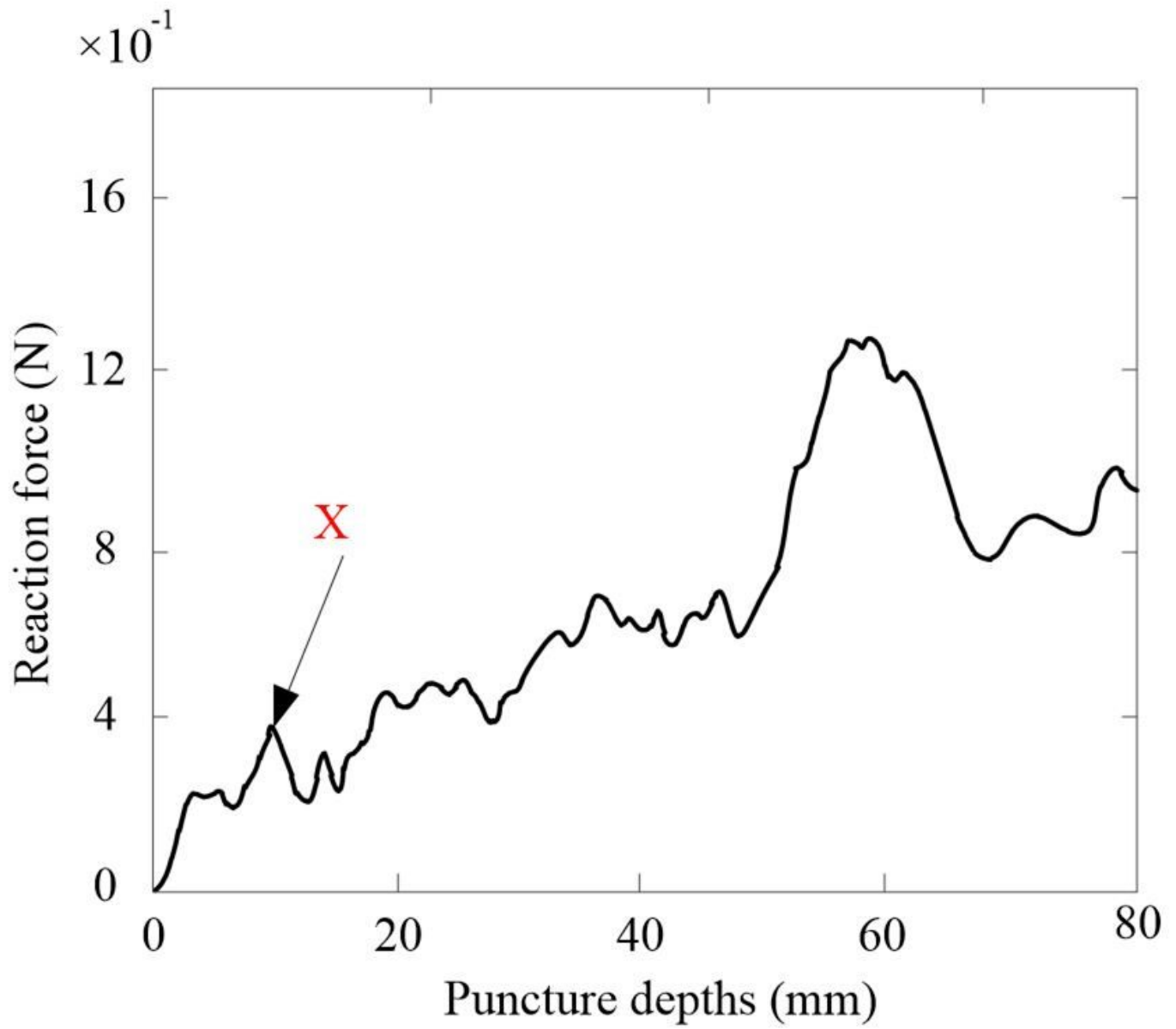


Figure 10

Reaction force of puncture needle at different puncture depths

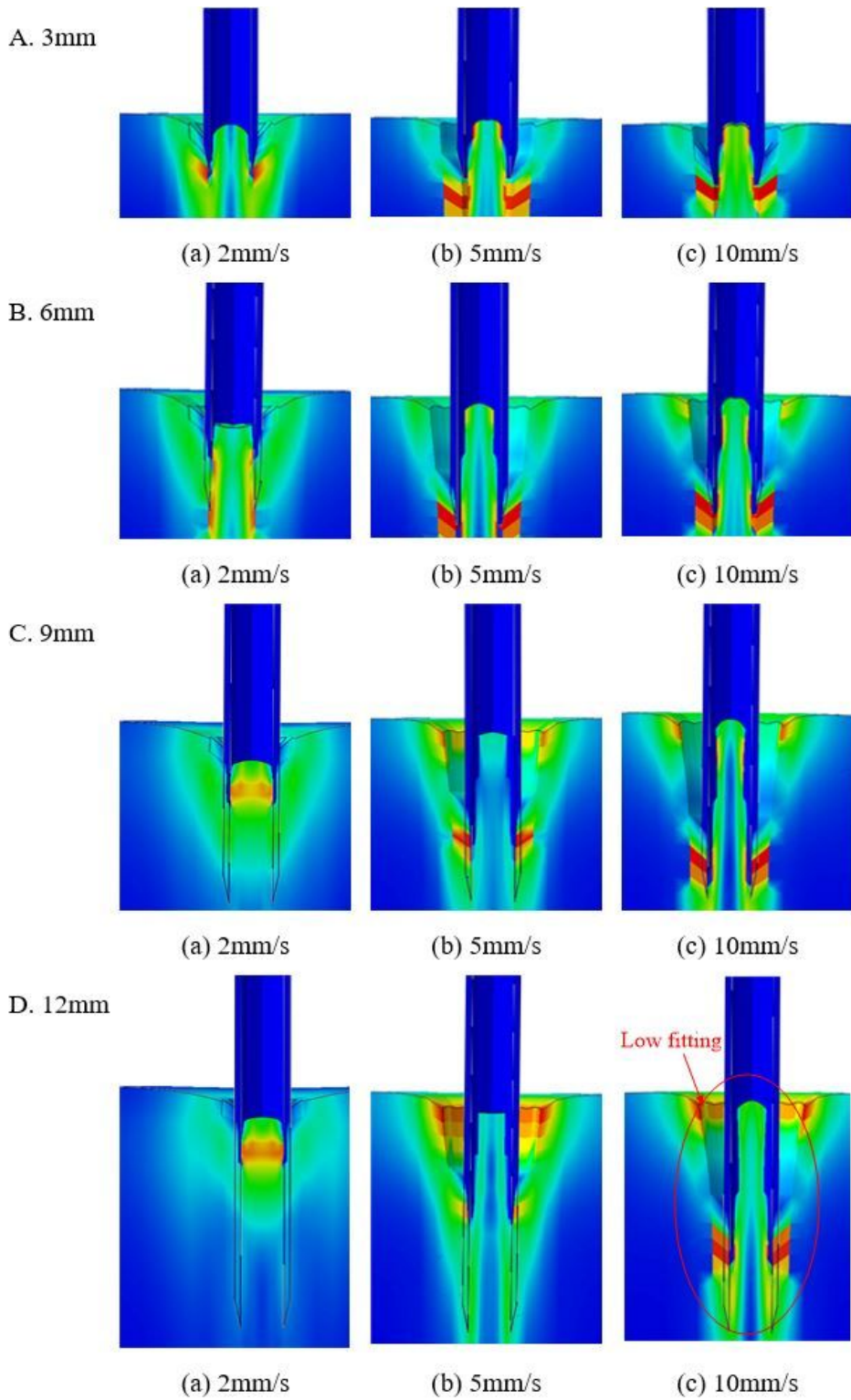
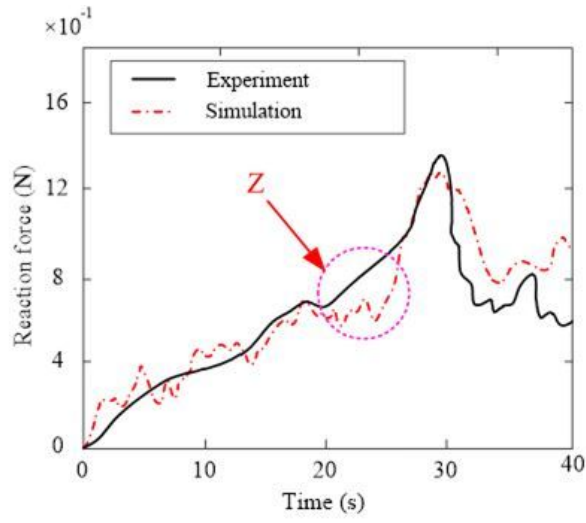


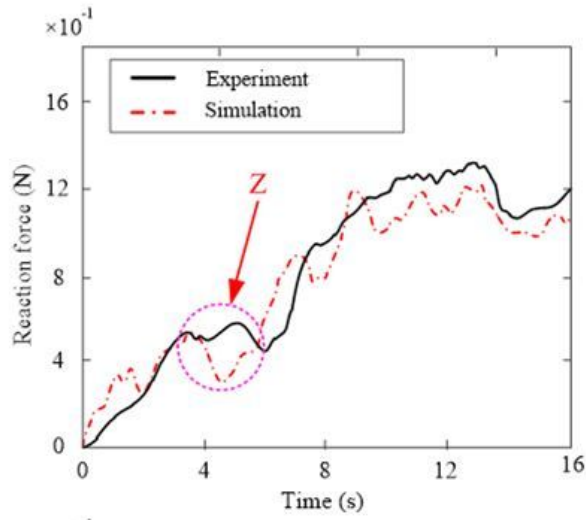
Figure 11

Stress changes at different puncture speeds at 3mm, 6mm, 9mm, 12mm

A. 2mm/s



B. 5mm/s



C. 10mm/s

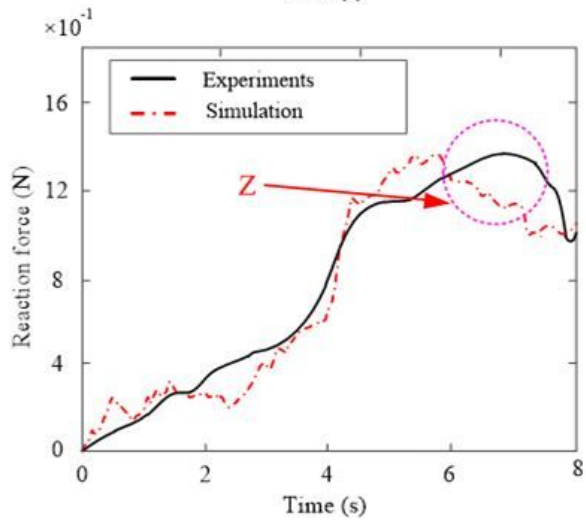


Figure 12

Reaction force of puncture needle at different puncture speeds